Experiments in Fluids (2022) 63: 136
https://doi.org/10.1007/s00348-022-03485-8

RESEARCH ARTICLE

A procedure for computing the spot production rate in transitional boundary layers

Matteo Dellacasagrande[1] · Davide Lengani[1] · Daniele Simoni[1] · Jan Pralits[2] · Kristina Durović[3] · Ardeshir Hanifi[3] · Dan Henningson[3]

Received: 11 February 2022 / Revised: 14 July 2022 / Accepted: 25 July 2022 / Published online: 17 August 2022

Abstract

The present work describes a method for the computation of the nucleation rate of turbulent spots in transitional boundary layers from particle image velocimetry (PIV) measurements. Different detection functions for turbulent events recognition were first tested and validated using data from direct numerical simulation, and this latter describes a flat-plate boundary layer under zero pressure gradient. The comparison with a previously defined function adopted in the literature, which is based on the local spanwise wall-shear stress, clearly highlights the possibility of accurately predicting the statistical evolution of transition even when the near-wall velocity field is not directly available from the measurements. The present procedure was systematically applied to PIV data collected in a wall-parallel measuring plane located inside a flat plate boundary layer evolving under variable Reynolds number, adverse pressure gradient (APG) and free-stream turbulence. The results presented in this work show that the present method allows capturing the statistical response of the transition process to the modification of the inlet flow conditions. The location of the maximum spot nucleation is shown to move upstream when increasing all the main flow parameters. Additionally, the transition region becomes shorter for higher Re and APG, whereas the turbulence level variation gives the opposite trend. The effects of the main flow parameters on the coefficients defining the analytic distribution of the nucleation rate and their link to the momentum thickness Reynolds number at the point of transition are discussed in the paper.

Davide Lengani, Daniele Simoni, Jan Pralits, Kristina Durović, Ardeshir Hanifi, Dan Henningson have contributed equally to this work.

✉ Matteo Dellacasagrande
matteo.dellacasagrande@edu.unige.it

[1] DIME, University of Genova, Via Montallegro 1, 16145 Genova, Italy

[2] DICCA, University of Genova, Via Montallegro 1, 16145 Genova, Italy

[3] FLOW, KTH Royal Institute of Technology, 10044 Stockholm, Sweden

Graphical abstract

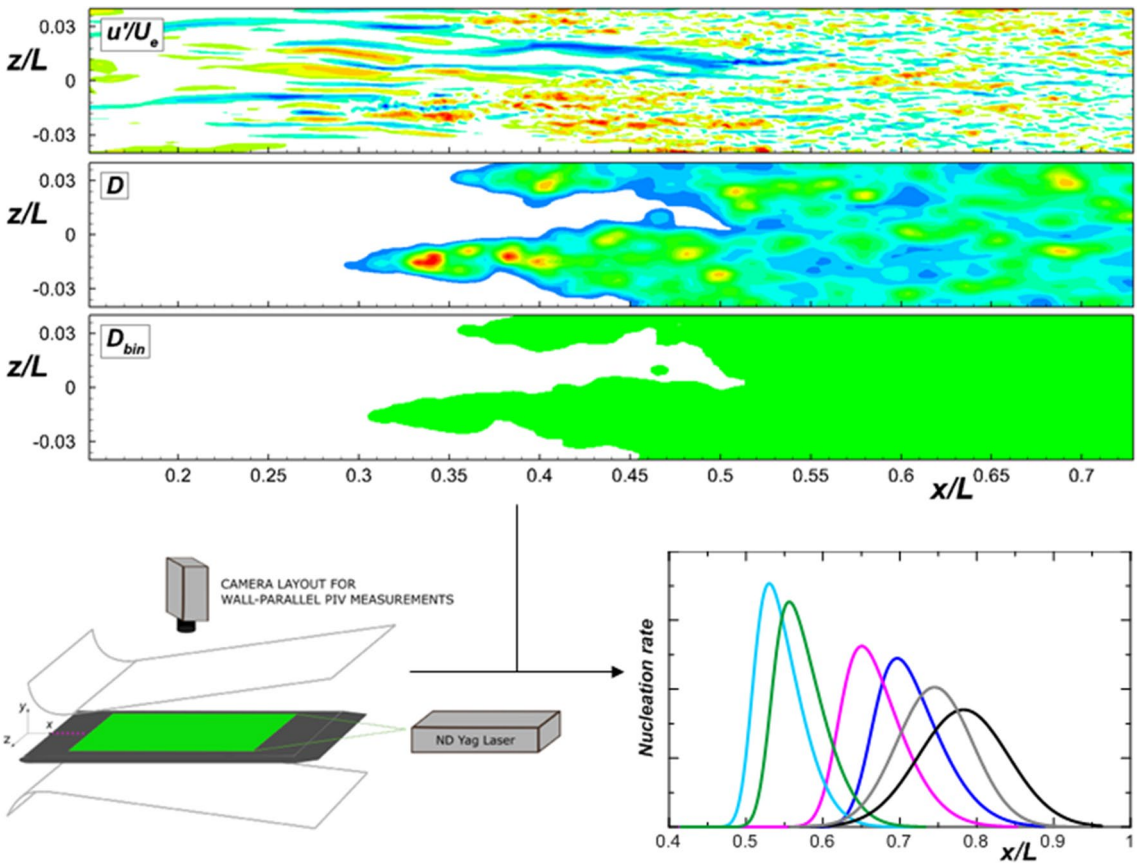

1 Introduction

The correct prediction of the laminar–turbulent transition of the boundary layer is of paramount importance for several engineering applications (see, e.g., Mayle (1991), Herbert (1991)). In this context, the identification of turbulent patterns, as well as the laminar–turbulent interface in the boundary layer, is a key factor for the characterization of all the intermittent flows (see among others Scarano et al (1999), Green et al (2007), Lee and Zaki (2018)). It is well known that under elevated free-stream turbulence, coherent elongated structures called streaks occur in the laminar boundary layer (Morkovin (1969), Matsubara and Alfredsson (2001), Brandt et al (2004) and Zaki (2013)) and then break up leading to the formation of turbulent spots (Emmons (1951)). Since the pioneering work of Emmons (1951), several researchers focused on the nucleation and the propagation of turbulent patches in the boundary layer (e.g., Narasimha et al (1984), Tillmark and Alfredsson (1992)), which grow causing transition to turbulence. Different techniques for turbulent events recognition were therefore proposed in the literature, whose usability strongly depends on the experimental environment and the available data (see, e.g., Richter et al (2016)). Early studies were based on the visual identification of transition, as from smoke wires, for instance (see, e.g., Batill and Mueller (1981)). Havener (1977) was among the first to use holography to detect boundary layer transition in supersonic high Reynolds number flows. Beside holography, optical interferometry was also adopted for the identification of the transition location based on density changes in the intermittent flows (see among others Azzazy et al (1989), Parziale et al (2013)). In more recent years, the infrared thermography has become a commonly adopted technique for the identification of transition since it does not require any special sensors or coatings (Richter and Schülein (2014), Gardner et al (2017)). Weiss et al (2020) investigated the unsteady transition on the blade suction side of a four-bladed sub-scale helicopter rotor by means of non-intrusive differential infrared thermography.

The authors reported noticeable agreement with the transition location highlighted by means of numerical simulations for the same flow case. Beside the optical techniques mentioned above, hot-wire probes and fast response pressure sensors are typically adopted to determine the boundary layer state with single point measurements (e.g., Siddiqui et al (2013), Ohno et al (2022)). Schulte and Hodson (1998) used signals from single hot-wire probe and surface-mounted hot-film gauges to investigate the turbulent patches originated from the wake boundary layer interaction in low-pressure turbine blades. Particularly, the variation of the shear stress was used for transition detection. Fransson et al (2005) used the velocity signal in the boundary layer measured with hot-wire probe, which was then high-pass filtered using a cut-off frequency that takes into account for the growth of the boundary layer. The threshold speed was determined based on the sensitivity of the intermittency function on the chosen threshold. The advancement of measuring techniques and numerical simulations provided an increased amount of data concerning transitional boundary layers in complex geometries and different flow conditions (see, e.g., Heisel et al (2018), Durović et al (2021)). In this context, the identification of the turbulent patterns and the laminar-turbulence interface in the boundary layer is typically obtained using specifically defined functions, thus providing the spatio-temporal distribution of turbulent spots. Among others, Nolan and Zaki (2013) considered the sum of the absolute values of the wall-normal and spanwise fluctuation fields. The detection function was sensitized and low-pass filtered and thresholding the filtered signal at each wall-normal location was done using Otsu's method (Otsu (1979)). Chauhan et al (2014) proposed a method based on the magnitude of the turbulent kinetic energy for the analysis of PIV data, that was successfully applied by Kwon et al (2016) among others. Kreilos et al (2016) used the local spanwise wall-shear stress at the wall for the analysis of data obtained from large eddy simulation (LES). In this case, the threshold was estimated from the probability density function of spanwise shear. Lee and Zaki (2017) chose the vorticity magnitude as the detector function, and threshold value comes from the probability density function of the logarithm of normalized vorticity magnitude at different heights from the wall. Reuther and Kähler (2018) compared three different techniques for the analysis of PIV images, based on the turbulent kinetic energy, the homogeneity of the non-turbulent flow regions, and the particle image density. A statistical analysis of the intermittency factor has revealed that the accurate detection is very sensitive to the threshold parameters for the turbulent kinetic energy and the homogeneity approaches. Simoni et al (2016) introduced a wavelet-based technique for detecting turbulent vortices in particle image velocimetry data. The intermittency function was computed based on the number of turbulent vortices detected in time at different spatial positions. Significant agreement was found between the intermittency distribution obtained from the above-mentioned technique and that obtained from hot-wire signals (see also the previous work of Collineau and Brunet (1993) for the use of wavelets in the analysis of intermittent signals). In the present work, we test different detection functions for turbulent events recognition using data from experiments and numerical simulation. More precisely, two functions based on velocity data taken at about half of the boundary layer thickness are compared with a function based on the local wall-shear stress, that was already adopted in the literature (Kreilos et al (2016)). The aim is to provide a tool for the identification of transition from experimental data from which the local wall-shear stress cannot be obtained. The capability of the different functions to capture the evolution of transition and the spatial distribution of nucleation events is first tested using data from direct numerical simulation. Then, particle image velocimetry measurements are analyzed to show the usability of the present method for the analysis of a data base concerning the variation of the Reynolds number, the free-stream turbulence intensity and the streamwise pressure gradient. Overall, 10 flow conditions were examined.

2 Experimental setup

2.1 Test section and data matrix

Measurements were performed in the open loop low-speed wind tunnel of the Aerodynamics and Turbomachinery Laboratory of the University of Genova. The test section consists of a flat plate with elliptic (4:1) leading-edge installed between two adjustable endwalls (see Fig. 1). This latter allows the modification of the streamwise pressure gradient imposed to the boundary layer. For the present experiments, the top end bottom endwalls have been set symmetrically so that all cases are tested with zero incidence. The test section has fixed converging geometry from the leading edge up to the geometric throat of the channel (located at $x/L = 0.2$), while the pressure gradient can be changed in the rear part of the plate. The plate is 300 mm long and 300 mm wide, and it is equipped with 51 pressure taps for measuring the overall loading distribution. Optical accesses on the side and the top walls of the test section allow performing PIV measurements with the laser sheet oriented both normal and parallel to the plate surface. For the present experiments, the opening angle of the top surface of the channel was set to 1, 3 and 5 degrees. The condition at 1 degree corresponds to

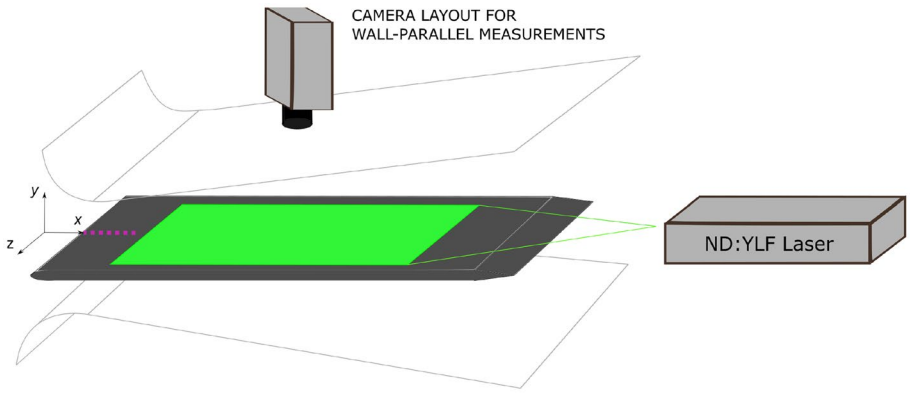

Fig. 1 Scheme of the test section and PIV instrumentation layout. The top and bottom endwalls are set symmetrically. PIV measuring plane is highlighted with green color. Violet dots indicate flush mounted pressure probes

Table 1 Acceleration parameter $AP = \frac{L}{U_{\infty,0}} \frac{\Delta U_\infty}{\Delta x}$ for the opening angle of the endwalls equal to 1 (ZPG), 3 (MPG) and 5 (SPG) degrees

ZPG ($\alpha = 1$)	MPG ($\alpha = 3$)	SPG ($\alpha = 5$)
0	– 0.9	–1.28

Table 2 Turbulence-generating grids characterization: free-stream turbulence intensity (Tu), bars width (d), mesh size (M), and porosity parameter $P = (1 - d/M)^2$

Re	Tu [%]	d [mm]	M [mm]	P
415k	2.5	2	8	0.64
415k	3.5	4	8	0.36
520k	2.5	2	8	0.64
520k	3.5	4	8	0.36

zero pressure gradient (ZPG) due to viscous blockage effects. Otherwise, the opening angles $\alpha = 3$ and 5 degrees correspond to a moderate (MPG) and a strong (SPG) adverse pressure gradient, respectively. A trip wire forcing transition of the endwalls boundary layer was used to avoid separation on these surfaces at the highest APGs. Table 1 reports the values of the acceleration parameter $AP = \frac{L}{U_{\infty,0}} \frac{\Delta U_\infty}{\Delta x}$ for the different angles tested, where L is the plate length, and $\frac{\Delta U_\infty}{\Delta x}$ is the overall velocity gradient across the diverging part of the channel. Here, ΔU_∞ is the difference between the free-stream velocity values probed at the channel throat (i.e., $U_{\infty,0}$) and the plate end. Note that by definition, AP does not depend on the flow Reynolds number.

The free-stream turbulence at the inlet of the test section was controlled using turbulence-generating grids with different geometries. The grids were located 500 mm upstream of the plate leading edge. The turbulence level measured at the plate leading edge varied in the range 2.5–3.5%. For the lowest turbulence intensity (Tu) level and the zero pressure gradient case, transition did not occur before the end of the plate. Then, for this condition, data are presented only for the highest Tu level. Details on the grid geometry and the FST characteristics are provided in Table 2. For the different Tu levels and pressure gradients, 2 Reynolds numbers based on the plate length and the free-stream velocity at the plate leading edge were considered ($Re = 415000, 520000$). The so-derived Reynolds number is used hereafter for the characterization of the different flow cases together with AP and Tu level. Otherwise, the momentum thickness Reynolds number will be adopted in the last section of the paper as a new axis on which to compute the probability density function of turbulent spot nucleation.

2.2 Measuring techniques

The boundary layer evolving on the top surface of the plate was surveyed by means of a Dantec time-resolved PIV system (maximum repetition rate of 5 kHz). Additionally, laser Doppler velocimetry (LDV) measurements were performed at different streamwise positions for the detailed characterization of the boundary layer integral parameters. The PIV measuring plane was located in the boundary layer, at a variable distance from the wall. Particularly, the laser sheet was inclined to be located at half of the boundary layer thickness at the inlet and the outlet sections of the measuring domain. The extension of the PIV frame in the spanwise direction was fixed to $z/L \approx 0.1$ in order to capture a sufficient number of alternating *high*- and *low*-speed streaks and breakup events. The streamwise position of the measuring domain was instead changed for the different cases in the region $0.3 < x/L < 1$, so that the entire transition process was captured for the different combinations of the flow parameters. PIV measurements were performed by seeding the flow with Vaseline oil droplets (mean diameter of 1.5 μm). The instrumentation adopted is constituted by a dual-cavity ND:YLF pulsed laser Litron LDY 300 (energy 30 mJ per pulse at 1000 Hz repetition rate, 527 nm wavelength). Optical lenses have been used to obtain a laser sheet with 1 mm thickness. The light scattered by the seeding particles

was recorded on a high-sensitive SpeedSense M340 digital camera with a cooled 2560 × 1600 pixels CMOS matrix. For the present experiments, the magnification factor was set to about 0.16. A multi-grid algorithm has been adopted for the computation of the adaptive cross-correlation of PIV images. A trial interrogation area of 32 × 32 pixels is used with a successive refinement to 16 × 16 pixels and 50% overlap. This corresponds to a vector grid spacing of 0.43 mm, which ensures that boundary layer streaks and their breakup events are well resolved even for the highest Reynolds number. With the PIV system operating in double frame mode, the time between laser pulses was chosen in order to achieve a particle displacement between the first and the second frames equal to 1/4 of the interrogation window size. For the present cases, the delay time of the laser pulses was in the range 5–12 µs, depending on the flow Reynolds number. A peak validation was used to discriminate between valid and invalid vectors. With this setting, a Gaussian fitting procedure guarantees a sub-pixel recognition accuracy of particle displacement of the order of 0.1 pixel. Based on the analysis reported in Sciacchitano et al (2015) and Wieneke (2015), the relative error in the evaluation of the instantaneous velocity is expected to be smaller than 3% for the present experiments. For each condition, eight independent sets of 2000 instantaneous velocity fields were acquired at a sampling rate of 1596 Hz. The detailed description of the experimental data and measuring techniques adopted in this work can be found in the authors' previous works Dellacasagrande et al (2021b), Verdoya et al (2021). For each flow condition, an LDV traverse was performed downstream of the channel throat (i.e., at $x/L = 0.3$) for the characterization of the velocity profile at the inlet section of the PIV measuring plane. This allowed the comparison between the experiments and the DNS results, as discussed in the following. Additional LDV traverses were also performed at the position of the maximum turbulent spot nucleation provided by the PIV measurements that corresponds to about the mid-transition position. In the present experiments, a four-beam laser Doppler velocimeter (Dantec Fiber Flow) was employed in backward scatter configuration. The LDV measuring volume has an ellipsoid shape, with the minor axes extending for 50 µm in the wall-normal and the streamwise directions, whit its major axis stretching 1.5 mm in the spanwise one. Each LDV traverse was constituted of 29 measuring points with the first one located at a distance of 50 µm from the wall. A measuring point spacing of 50 µm was adopted up to 1 mm from the wall, while the measuring grid is coarser in the outer part of the boundary layer. For each measuring point, the acquisition period was set to 120 s to ensure the convergence of the statistical moments. The data rate was of the order of 10 kHz away from the wall, but it was significantly lower in the close to the wall region. However, the acquisition period of 120 s provided a sufficient number of data for statistics also for the measuring points in proximity of the plate surface. Statistical moments were weight-averaged with seeding particle transit time to reduce the statistical bias. The statistical uncertainty in the evaluation of the mean flow velocity is estimated to be lower than 2%, while it increases to around 4% for the fluctuating velocity rms (see the previous work by Satta et al (2007) for further details).

3 Direct numerical simulation

The geometry and the mean flow parameters of the numerical simulations follow closely those used in the experiments by Fransson and Shahinfar (2020). Details of simulations can be found in Durović (2022). The flow of an incompressible fluid with uniform properties is analyzed using Navier–Stokes equations

$$\frac{\partial \mathbf{u}}{\partial t} + \mathbf{u} \cdot \nabla \mathbf{u} = -\nabla p + \frac{1}{Re} \nabla^2 \mathbf{u} + \mathbf{f}, \quad \nabla \cdot \mathbf{u} = 0 \tag{1}$$

where $\mathbf{u} = \{u, v, w\}^T$ represents the velocity vector, p is the pressure, and $\mathbf{f}$ is the body force. The numerical tool used for the simulations is the Nek5000 (Fischer et al 2021) code which is based on a spectral-element method (Patera 1984). The spatial discretization is done using the Galerkin approximation, following the $\mathbb{P}_N - \mathbb{P}_{N-2}$ formulation. The solution is interpolated within a spectral element employing Lagrange interpolants of orthogonal Legendre polynomials on the Gauss-Lobatto-Legendre quadrature points. The non-linear terms are treated explicitly by third-order extrapolation, whereas the viscous terms are treated implicitly by a third-order backward differentiation scheme. Dealiasing of the non-linear terms is performed using overintegration. First, a DNS of a laminar case without any perturbations in the flow is simulated using boundary conditions corresponding to the experimental setup by Fransson and Shahinfar (2020). As inflow, we use Dirichlet boundary conditions. In the spanwise direction, a periodic condition is enforced, while at the wall, the velocity field is subjected to a no-slip condition. The outflow conditions are the following

$$\frac{1}{Re}\frac{\partial u}{\partial x} - p = 0, \qquad \frac{\partial v}{\partial x} = 0, \qquad \frac{\partial w}{\partial x} = 0 \tag{2}$$

and on the top boundary, we employ

$$u = U_\infty, \qquad \frac{1}{Re}\frac{\partial v}{\partial y} - p = 0, \qquad w = 0 \tag{3}$$

where the first boundary condition in Eq. 2 and the second in Eq. 3 are asymptotic conditions that are normally adopted for the Galerkin approach to the Navier–Stokes equations, as for the present case (Ol'Shanskii and Staroverov 2000). The

grid resolution at the plate surface varies with the streamwise location, with $\Delta x^+ = 0.2 - 6$. The smallest y^+ is 0.3 on the plate surface, and this increases through the boundary layer. Resolution in the spanwise direction is $\Delta z^+ = 4$.

In the present case, the isotropic and homogeneous free-stream turbulence is prescribed in a volume section close to the inlet boundaries through a volume forcing. The free-stream turbulence is obtained as a superposition of Fourier modes with a random phase shift, which have been added to the forcing vector. A general disturbance field can be written as

$$u_i(x,y,z,t) = \sum_{k_x,k_y,k_z,\omega} A\hat{u}(k_x,k_y,k_z,\omega)e^{i(k_x x+k_y y+k_z z-\omega t)} \tag{4}$$

where A represents the scaled amplitude of the free-stream modes, k_x, k_y, k_z are the streamwise, wall-normal and spanwise wavenumbers, respectively, and ω is the angular frequency of the Fourier modes. Further, Taylor's frozen hypothesis is used to relate the temporal scale of the modes to their streamwise scale through relation $\omega = k_x U_\infty$. In practice, we truncate the sum in equation (4) by considering modes whose wavenumber vectors (k_x, k_y, k_z) have an amplitude between given minimum and maximum values (k_{min} and k_{max}, respectively). Then, the portion of wavenumber space with amplitude between k_{min} and k_{max} is divided into a set of concentric shells, each containing 20 wavevectors with the same length. The amplitude of the free-stream modes on each spherical shell is scaled using the von Kármán spectrum given by the relation

$$E(\kappa) = \frac{2}{3}\Lambda \frac{1.606(\kappa\Lambda)^4}{\left[1.350 + (\kappa\Lambda)^2\right]^{17/6}} q. \tag{5}$$

Here, Λ represents the integral length scale, and q is the total turbulent kinetic energy. Note that the length scale defined from the longitudinal two-point correlation is related to Λ as

$$\Lambda_{11} = \int_0^\infty \frac{\overline{u(x)u(x+r)}}{\overline{u(x)^2}} dr \approx 0.643\Lambda. \tag{6}$$

The method described above allows us to investigate the effects of the integral length scale and turbulence intensity of the free-stream turbulence on the boundary layer transition. The investigated integral length scales were 11.53, 20.39 and 29.22mm. The case $\Lambda = 11.53mm$ was used for comparison with the experiments, with Tu=3.4%. A similar method for the generation of free-stream turbulence has been used in Schlatter (2001) and Brandt et al (2004).

4 Detection functions for turbulent events recognition

In this section, PIV and DNS data are used to develop and validate a procedure for turbulent events recognition. Several detection functions (hereafter named D) were tested in this work and then applied to the present data set for the computation of the intermittency function and the rate of turbulent spot nucleation. Three different functions among the overall tested are presented and compared using data from direct numerical simulation described in Sect. 3. Two detection functions based on velocity data taken at about half of the BL height are compared with a function based on the local spanwise wall-shear stress, which is adopted in the previous work of Kreilos et al (2016). The current analysis is therefore aimed at identifying and validating a detection function for tracking turbulent events when velocity data for the computation of the wall-shear stress are not available (as for PIV data). The functions here discussed are listed below:

$$D_w = w' \tag{7}$$

$$D_\Delta = w'\left(\frac{\partial w'}{\partial x} + \frac{\partial w'}{\partial z}\right) \tag{8}$$

$$D_\tau = \left(\frac{\partial w'}{\partial y}\right)_{y=0} \tag{9}$$

Note that the functions defined in equations (7-9) are all based on the spanwise component of the perturbation velocity w'. Indeed, pre-transitional flows are dominated by streamwise velocity fluctuations due to the occurrence of boundary layer streaks (Mans et al (2005), Matsubara and Alfredsson (2001)). Otherwise, turbulent events are characterized by strong cross-flow oscillations and spanwise wall-shear stress (see, e.g., Nolan and Zaki (2013), Kreilos et al (2016)). High values of the functions (7-9) are therefore linked to the occurrence of turbulent events, while they are almost null in the laminar BL, as discussed in the following. It is stressed here that the function D_τ proposed by Kreilos et al (2016) for the analysis of numerical data is taken as reference for the validation of D_w and D_Δ, which can be easily computed from PIV measurements.

Once the quantities are given in equations (7-9) were computed for all the time instants and spatial positions, their spatial root mean square (rms) was computed over a moving cell of 5×5 measuring points. The so-derived rms value was then assigned for each cell to the corresponding center point (see the scheme reported in Fig. 2). This allowed us to further highlight the incoherent fluctuations occurring in turbulent regions, where the rms of turbulent quantities is known to increase. It is stressed here that the choice of the

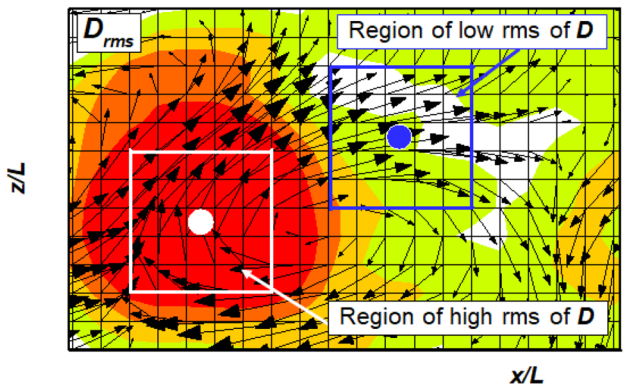

Fig. 2 Zoomed view of the contour plot of the rms of D_w (subscript *rms*) obtained from PIV data. The extension of the 5×5 points cell adopted for the computation of the rms of D_w is indicated. Two cells with low and high rms of D_w are highlighted with blue and white colors, respectively

cell size depends on the spatial resolution and flow scales. In this context, a cell size sensitivity analysis has been done using DNS data. Cells of different dimensions have been found to provide similar results, which are not shown here for brevity. The discussion presented hereafter therefore refers to the local rms values of the detection functions (7-9), that were computed over a 5×5 points grid. To better distinguish between laminar and turbulent regions, a discrete laminar–turbulent representation of the flow has been computed based on the functions (7-9). To this end, the procedure described in the pioneering work of Otsu (1979) has been used. More precisely, the values assumed by each detection function were grouped in two distinct classes, where the threshold is set to minimize the inter-class variance. The values of the functions (7-9) that are higher than the threshold indicate the occurrence of turbulent events, whereas lower values are linked to laminar ones. This procedure provides binary maps (0-*laminar*, 1-*turbulent*) which are then used for the computation of the intermittency function (see Narasimha et al (1984)) by integration on both the spanwise and the temporal coordinates. Indeed, the present procedure provides sigmoid-like curves which have null value in the laminar region, while they are equal to one where the boundary layer reaches the fully turbulent state.

The intermediate steps of the above-presented method are synthesized in Fig. 3. The first plot shows an instantaneous contour map of the streamwise perturbation velocity obtained from the DNS data at about $y/\delta_{99} = 0.5$ (δ_{99} is the BL thickness). Elongated structures are clearly recognizable in the first part of the domain, which resemble *high*- and *low*-speed streaks. Otherwise, turbulent events, that are characterized by sensibly smaller scales, are observable for $x/L > 0.25$ at different spanwise positions (see, e.g. the finer scale structures forming at $x/L = 0.28$ and $z/L = -0.012$, with L being the plate length). Downstream of $x/L = 0.5$, streaks are completely disrupted, and turbulent fluctuations dominate. These latter are characterized by high values of the spanwise fluctuating velocity (second plot), while smaller ones are observed in the regions where ordered streaks occur. This highlights the usability of w' as ingredient for the construction of detection functions for turbulent event recognition.

The successive plots of Fig. 3 depict the spatial distribution of the normalized detection functions D_τ, D_w and D_Δ together with their discrete laminar–turbulent representations (subscript *bin*). It should be noted that high values of all the functions here tested are observed at the same positions where turbulent fluctuations occur in the first and second plots of Fig. 3. More precisely, the signatures of two turbulent spots forming at about $x/L = 0.28$ and $x/L = 0.35$ are captured by the functions D_τ, D_w and D_Δ. Otherwise, smaller values of these functions are obtained at the spatial positions where ordered streaks occur, as for the elongated low-speed streak extending up to $x/L = 0.5$ at $z/L = 0.018$. This clearly indicates the capability of the present procedure to isolate turbulent regions from the laminar ones. Downstream of $x/L = 0.55$, where the boundary layer is almost turbulent (see the second plot), the functions D_τ and D_w show the highest values and spatial homogeneity, while lower ones are observed for the function D_Δ. For this reason, the function D_w will be adopted in the following for the analysis of the PIV data. The last three plots of Fig. 3 show the discrete laminar–turbulent representation of the functions (7-9) obtained by means of the Otsu's method Otsu (1979). The laminar–turbulent interface in the boundary layer is clearly identified by the three detection functions herein presented. Interestingly, the functions D_w and D_Δ provide substantially the same laminar–turbulent representation as for D_τ, thus allowing the identification of turbulent spots in the boundary layer.

To compute the rate of turbulent spots nucleation, the streamwise coordinate of all the measuring points belonging to the laminar–turbulent interface was recorded first. Then, the points with local minimum values of the streamwise abscissas were associated with the inception of new turbulent spots (see the red circles in Fig. 4). The number of nucleation events (N) divided by the spanwise length of the domain (L_z) and the overall period of observation (T) finally provided the spot production rate (n) in its dimensional form.

To prove the usability of the functions D_w and D_Δ for the identification of transition, the intermittency curve and the spatial distribution of the spot production rate ($n = N/L_z T$) were computed from the DNS data and are shown in Fig. 5 together with those obtained from the function D_τ. For each streamwise position, the intermittency is computed as the spanwise averaged value of the number of turbulent points of each record (i.e., the green ones shown in Fig. 4) divided by the number

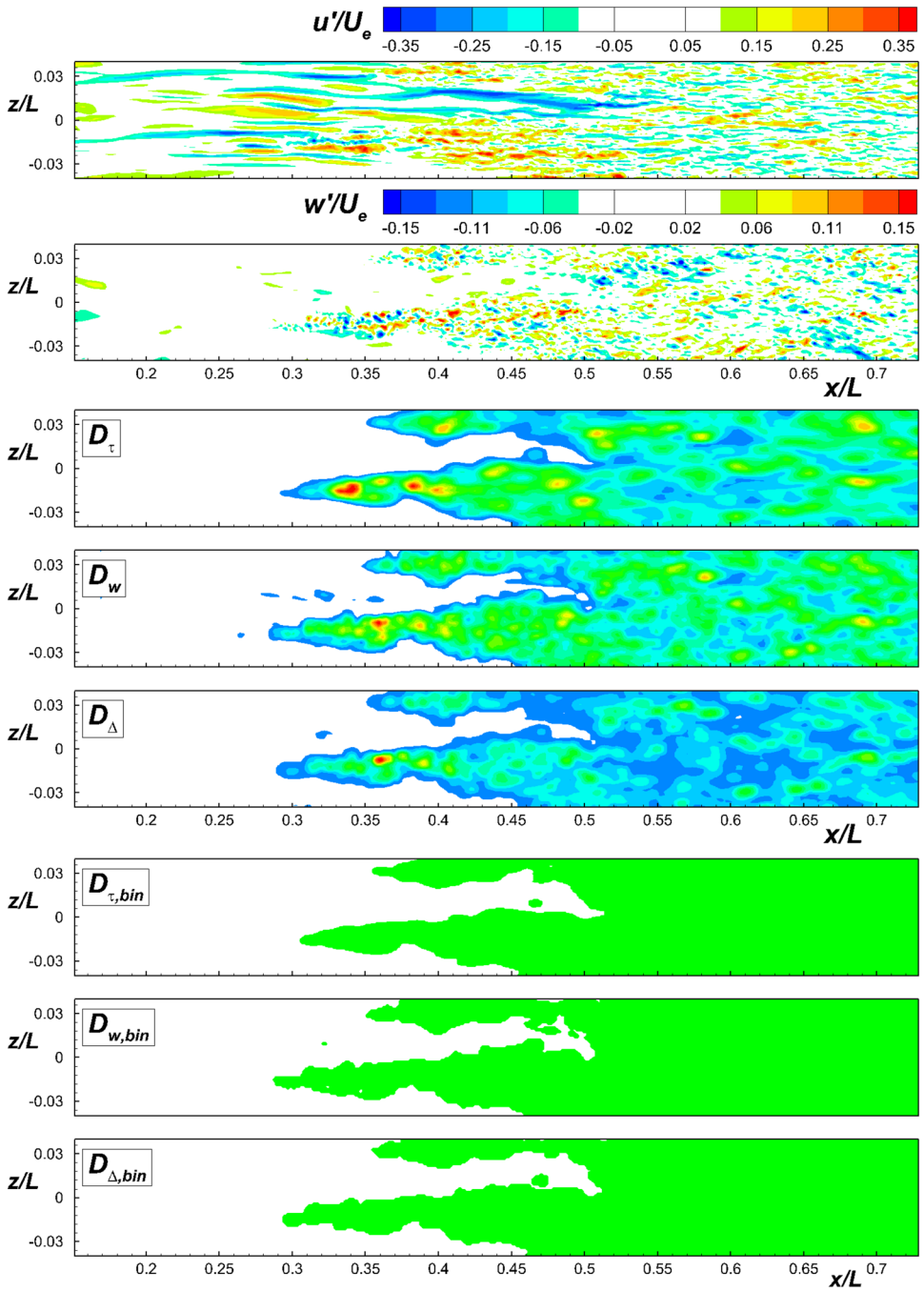

Fig. 3 Top-view of flat plate boundary layer obtained from DNS. First and second plots: contour plot of streamwise and spanwise perturbation velocities scaled with free-stream velocity U_e. Third to fifth plots: normalized detection function D_τ, D_w and D_Δ. Sixth to eighth plots: binary map of the detection functions obtained by means of Otsu's method. Streamwise and spanwise coordinates are scaled with the plate length

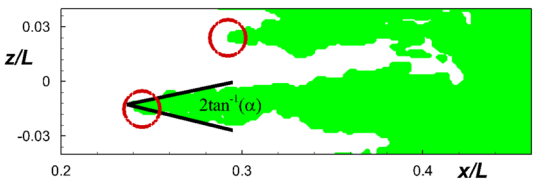

Fig. 4 Identification of turbulent spot nucleation from DNS data. Nucleation positions are indicated with red circles, while black lines indicate the spot spreading angle

of snapshots. This directly gives the fraction of time for which the BL is turbulent at different streamwise locations. It is worth noticing that the intermittency distributions obtained from the three detection functions are substantially superimposed one another. Slightly higher values are observed at the beginning of transition for the function D_w. However, the peak value of the nucleation rate as well as its streamwise location is substantially the same for all cases (see the bar-plots in Fig. 5). As a consequence, accurate distributions of the intermittency function and of the spot production rate can be computed from

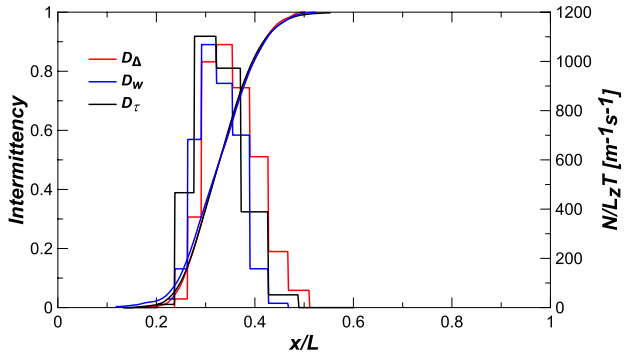

Fig. 5 Intermittency curves and nucleation rate distributions obtained from DNS data for different detection functions: red, blue and black lines are obtained using the detection functions D_{Δ}, D_w and D_{τ}, respectively

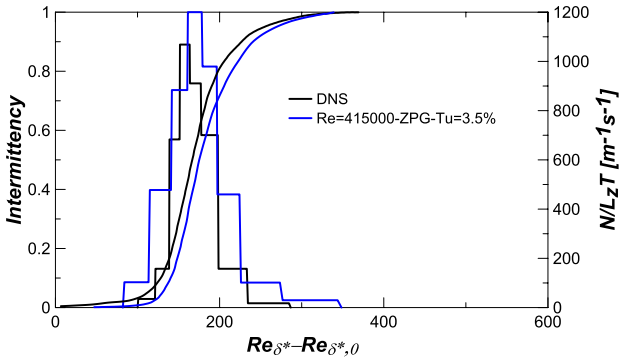

Fig. 6 Comparison of intermittency and nucleation rate distributions obtained from the DNS data (black line) and the PIV measurements (blue line) for $Re = 415000$, zero pressure gradient and Tu=3.5%

experimental data from which the local wall-shear stress cannot be directly obtained, as further discussed in section 4.1. With the aim of highlighting the link between the nucleation rate obtained from the present procedure and the slope of the corresponding intermittency distribution, the non-dimensional spot production rate (Narasimha et al (1984)) defined as:

$$\hat{n} = \frac{n\sigma\nu^2}{U_e^3} \tag{10}$$

was computed from the DNS data using D_w as detection function. Note that n in the equation above provides an estimate for the nucleation rate computed in this work being defined as the number of nucleation events per unit time and spanwise length. The coefficient σ is the non-dimensional spot propagation parameter introduced first by Emmons (1951):

$$\sigma = \alpha^2\lambda/\beta \tag{11}$$

where α and λ are spot geometrical parameters, and β is the propagation velocity of turbulent spots. According to the pioneering work of Narasimha et al (1984), the slope of the linear fit to the function $F(\gamma) = [-ln(1-\gamma)]^{0.5}$ plotted versus the local Reynolds number $Re_x = xU_e/\nu$ directly provides the non-dimensional spot production rate as defined in equation (10). Once applied to the intermittency distribution depicted in Fig. 5, the procedure here mentioned provided a value for $\hat{n}$ equal to 2.54E-10. Then, the dimensional nucleation rate n was computed from equation (10) once the coefficients α, λ and β were estimated based on the present DNS data. The above-mentioned coefficients were found to be equal to 0.17, 0.45 and 0.64, respectively, in good agreement with the previous literature works of Emmons (1951) and Gostelow et al (1992). With these values, a dimensional spot production rate $n = 1180$ has been obtained by inverting equation (10), which is strictly comparable to the peak values of the distributions reported in Fig. 5. Therefore, the present procedure allows capturing the actual rate of turbulent spot nucleation that agrees well with the statistical evolution of transition based on the intermittency curve.

4.1 Comparison of DNS and PIV results

In order to further test the reliability of the procedure presented above and to verify its usability for the present data set, the intermittency function and the nucleation rate distributions obtained from the PIV measurements were compared with those obtained from the DNS data for similar inlet conditions. More precisely, the case $Re = 415000$, zero pressure gradient and $Tu = 3.5\%$ was used for comparison with the DNS results. For this experimental condition, the displacement thickness Reynolds number measured at $x/L = 0.3$ (i.e., just downstream of the channel throat) was found to be similar to that computed from the DNS data near the leading edge of the plate (i.e., $Re_{\delta^*,0} = 330$). Figure 6 provides the comparison between the intermittency and the nucleation rate distributions obtained from the DNS and the PIV measurements based on the detection function D_w (Eq. 7). The curves are plotted versus the non-dimensional streamwise coordinate defined as the difference between the local displacement thickness Reynolds number and the reference value $Re_{\delta^*,0} = 330$. This directly allows the comparison of the numerical and the experimental data. The results presented in Fig. 6 indicate that, for comparable inlet conditions, the present procedure provides quite similar distributions within a good level of approximation, despite the accelerating part in the experiments. Particularly, transition starts at about $Re_{\delta^*} - Re_{\delta^*,0} = 100$ and it ends at about $Re_{\delta^*} - Re_{\delta^*,0} = 350$ for both the DNS and the PIV data. Additionally, the peak value of the nucleation rate and its streamwise position are comparable for simulation and experiments. In the next section, the detection function D_w will be applied to the present data set to identify the

statistical response of the transition process to the modification of the main flow parameters.

5 Computation of nucleation rate from PIV measurements

5.1 Coherent structures in the boundary layer

Before discussing the effects due to the systematic variation of the main flow parameters, exemplary PIV snapshots are presented to show the main structures governing the transition process of the boundary layer. Particularly, the modification of the inlet turbulence was found to have significant effects on the dominant structures driving the laminar–turbulent transition. Figures 7 and 8 show wall-parallel PIV snapshots for the cases $Re = 415000$, MPG, Tu=2.5% and $Re = 415000$, MPG, Tu=3.5%, respectively. In each plot, the perturbation velocity vectors are superimposed to the contour plot of the streamwise fluctuating velocity scaled with the free-stream time-averaged value. For the low Tu case (Fig. 7), the transition process is driven by the amplification and the successive breakup of elongated streaky structures. In the first snapshot of Fig. 7, alternating *high*− and *low*−speed streaks are observed for $0.72 < x/L < 0.81$. In the successive time instants, streaks propagate downstream and they finally break up for $x/L > 0.85$, where wall-normal vorticity nuclei occur. Interestingly, for the case with Tu=3.5% (Fig. 8), large-scale spanwise-oriented structures are instead observed in the first half of the measuring plane. The occurrence of such kind of large-scale structures is linked to the modification of the FST characteristics, as discussed also in the work of Ovchinnikov et al (2008). The horizontal stripes observed in the first plot of Fig. 8 show spanwise oscillations in the successive PIV snapshots (see, e.g., the second and the third plot at $x/L = 0.65$) and finally break up for $0.65 < x/L < 0.7$ (see the last plot). As shown in Sect. 5.2, the turbulent events recognition technique presented here will correctly capture the anticipation of transition due to the modification of the FST characteristics, regardless of the different structures driving the transition process of the boundary layer.

5.2 Computation of the intermittency and the nucleation rate distributions

The procedure described in Sect. 4 is here applied to the present data set to show its capability of capturing the effects due to the Re, Tu level and pressure gradient variation on the transition process. The streamwise distribution of the nucleation rate $n = N/L_z T$ computed from the PIV measurements was fitted using a skewed Gaussian function to provide the probability density function (*pdf*) of the spot production rate:

$$pdf(n) = 2\phi(x, \mu, \sigma)\Phi(x, \mu, \sigma, \eta) \tag{12}$$

with,

$$\phi(x, \mu, \sigma) = \frac{1}{\sigma\sqrt{2\pi}} exp\left(-\frac{(x-\mu)^2}{2\sigma^2}\right) \tag{13}$$

and,

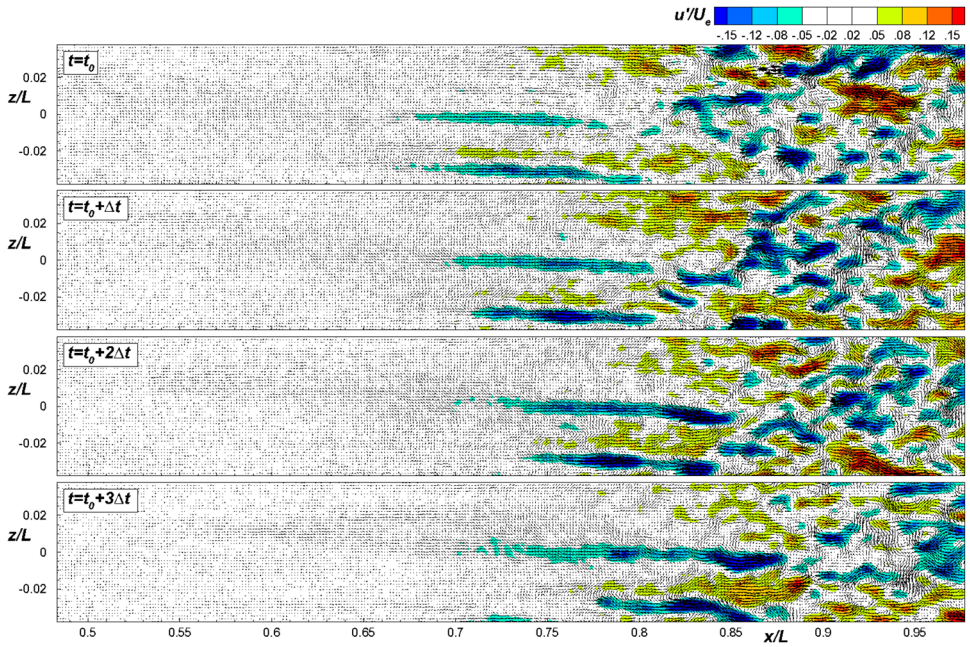

Fig. 7 PIV realizations for the case Re=415000, MPG and $Tu = 2.5\%$. Perturbation velocity vectors are superimposed to the contour plot of the streamwise fluctuating velocity scaled with the local time-averaged free-stream value. Streamwise and spanwise coordinates are scaled with the plate length. The time increment between successive snapshots is $\Delta t = 0.00062s$

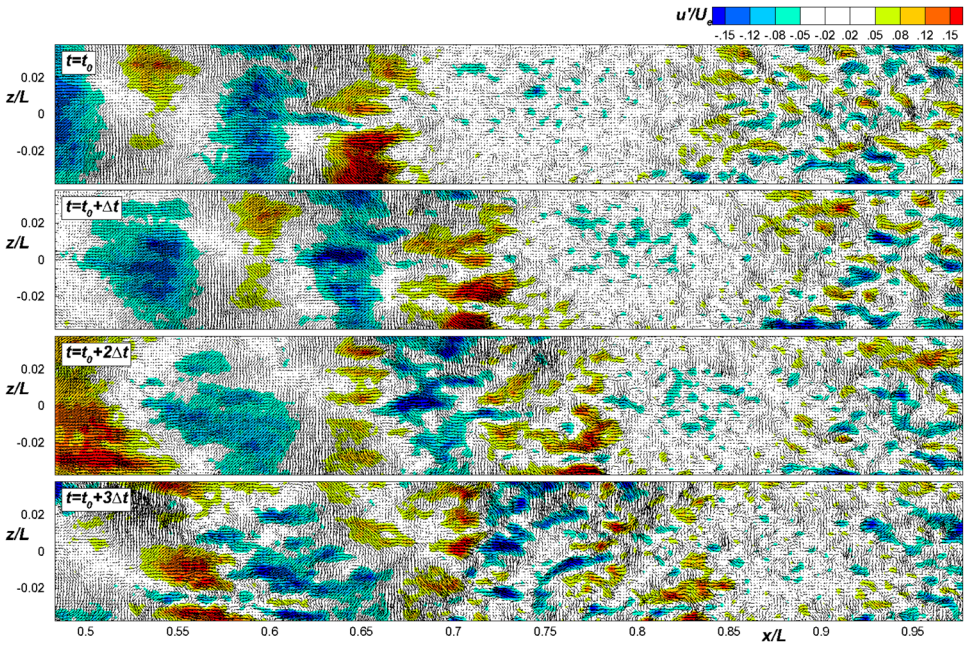

Fig. 8 PIV realizations for the case Re=415000, MPG and $Tu = 3.5\%$. Perturbation velocity vectors are superimposed to the contour plot of the streamwise fluctuating velocity scaled with the local time-averaged free-stream value. Streamwise and spanwise coordinates are scaled with the plate length. The time increment between successive snapshots is $\Delta t = 0.00062s$

$$\Phi(x,\mu,\sigma,\eta) = \frac{1}{2}\left[1 + erf\left[\eta\left(\frac{x-\mu}{\sqrt{2}\sigma}\right)\right]\right] \tag{14}$$

erf in equation (14) indicates the Gauss error function, while μ, σ and η define the mean, the variance and the skewness of the *pdf* distribution, respectively. Therefore, equation (12) defines a skewed Gaussian distribution with unit area, which is strictly linked to the fitting function adopted in the previous work of Kreilos et al (2016). The above coefficients were found by minimizing the L_2 norm of the error between the measured values of the nucleation rate and the analytic distribution defined in equation (12). This provided the best fit to the present data set with the minimum coefficient of determination (R^2) equal to 0.978 for all cases.

Figure 9 shows the fitting curves obtained from the PIV measurements, which are plotted versus the non-dimensional streamwise coordinate x/L. This allows the direct inspection of the effects due to the flow parameters on the statistical evolution of transition. Successively, equation (12) will be used to fit the nucleation rate distributions once plotted versus the local momentum thickness Reynolds number (Re_θ). This latter parameter is indeed typically adopted in the literature as indicator of the transition onset position, being also the main ingredient, beside the Tu level, of most of the existing correlations for the transition onset prediction (see among others Mayle (1991); Abu-Ghannam and Shaw (1980); Gostelow et al (1992); Menter et al (2006); Dick and Kubacki (2017)).

Figure 9a depicts the intermittency and the *pdf* of nucleation rate for different Reynolds numbers and pressure gradients at constant Tu=3.5%. The effects of varying the free-stream turbulence intensity are instead presented in Fig. 9b for the intermediate pressure gradient and different Reynolds numbers. The black curves depicted in Fig. 9a refer to the same case presented in section 4.1 (i.e., Re = 415000,

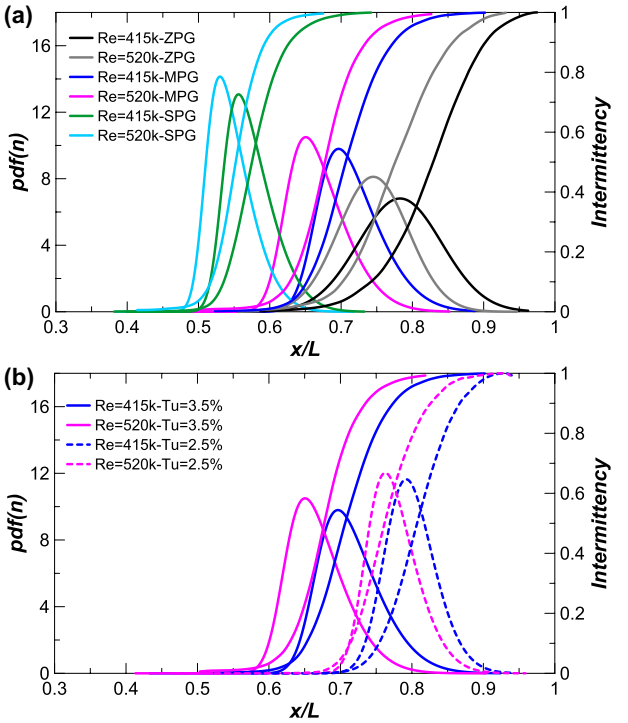

Fig. 9 Intermittency and *pdf* of nucleation rate obtained from PIV data: (a) Reynolds number and pressure gradient effects at fixed Tu=3.5%; (b) Tu level effects at variable Reynolds number and constant pressure gradient (MPG)

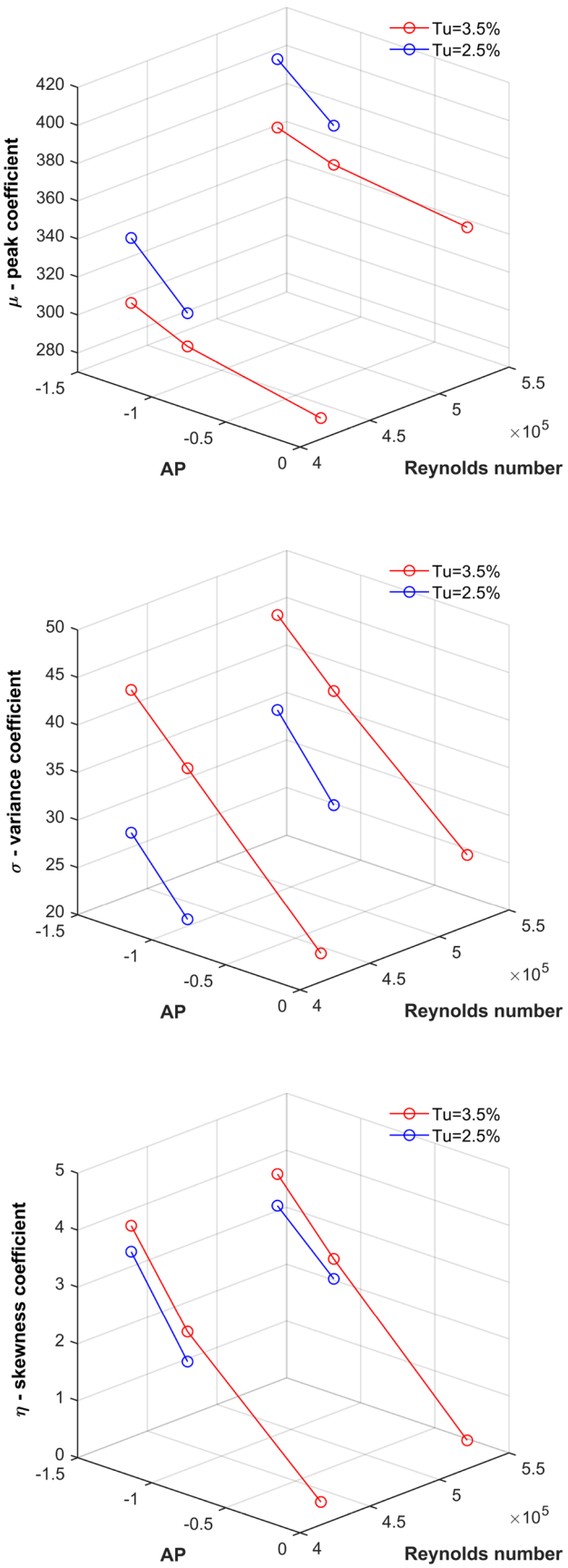

Fig. 10 Effects of Re, acceleration parameter and *Tu* level on the peak (μ, top plot), variance (σ, mid plot) and skewness (η, bottom plot) coefficients. Red and blue symbols refer to *Tu* level equal to 3.5% and 2.5%, respectively

ZPG, $Tu = 3.5\%$). As the Reynolds number and the APG increase, the onset of transition moves upstream and the transition region is shortened (i.e., the intermittency curve becomes steeper). The greatest effects in this sense are due to the increment of the adverse pressure gradient (Dellacasagrande et al 2020). Accordingly, the maximum peak of the *pdf* of the nucleation rate moves significantly upstream for the higher APGs and the peak value increases. On the contrary, the increment of the APG leads to lower variance of the *pdf*, which exhibits a marked right skewness. This means that when the APG increases, most of turbulent spots are formed in a narrow streamwise window within the transition region, while the number of nucleation events slowly reduces as the boundary layer approaches the turbulent state (see also the previous works by Nolan and Zaki (2013) and Dellacasagrande et al (2021a)).

Figure 9b shows the response of the transition process to the modification of the free-stream turbulence. The dashed lines refer to the cases at Tu=2.5%, whereas the continuous lines are the same presented in Fig. 9a for the MPG condition. As the Tu level is reduced, the transition onset position moves downstream, as expected, and the nucleation peak increases. It is stressed here that since all the *pdf* distributions have unitary area, higher peak values are directly linked to the narrowing of the transition region. As previously shown in Fig. 7 and 8, different structures, whose breakup occurs at different streamwise positions, drive the transition process of the boundary layer for these two free-stream turbulence conditions. More precisely, for the case at Tu=3.5%, spanwise-oriented structures were observed, whose breakup occurs at different spatial positions with respect to the streak breakup events observed for the low Tu case. It is worth noticing that the peak of the blue solid curve occurs at the same position at which the breakup events of the spanwise-oriented structures are observed in Fig. 8. This latter therefore drives the boundary layer transition, which is well captured by the procedure here discussed. Additionally, the increased variance and right skewness observed for the high Tu level suggest that turbulent spots are formed in a wider spatial region and are probably due to the complementary action of BL streaks and spanwise-oriented structures.

In order to synthesize the effects of Re (based on plate length), APG and Tu level variation on the coefficients μ, σ and η defining the *pdf* of turbulent spot nucleations, these quantities are plotted in Fig. 10 for all the combinations of the flow parameters. Additionally, the coefficients above mentioned were computed by means of non-linear fitting to the experimental *pdf*s plotted versus Re_θ. As previously mentioned, this allowed us the comparison with the previous literature works concerning with transition prediction and modeling. Particularly, the peak coefficient (μ) provides the value of Re_θ at about the mid-transition position (i.e., at the *pdf* peak), while σ provides the length of transition expressed as Re_θ variation across the transition region (i.e., $6\sigma \approx \Delta Re_\theta$ across transition). Otherwise, the coefficient η is a *pdf* shape parameter, and thus, it keeps the same values regardless of the coordinate adopted for the fitting.

The top plot of Fig. 10 shows the effects of Re (based on plate length), the pressure gradient and the Tu level on the peak coefficient μ. The value of Re_θ at the *pdf* peak location is only slightly affected by the pressure gradient variation, especially at the highest Tu level (see the previous work of Abu-Ghannam and Shaw (1980)). When lowering the Tu level, the μ coefficient increases (see the blue symbols), and so the value of Re_θ at the *pdf* peak, which is in good agreement with the past literature work of Mayle (1991), for instance. Sensibly larger values of μ, thus of Re_θ, are instead observed when increasing the flow Reynolds number, which is directly linked to the increment of Re_θ at the inlet section of the diverging part of the channel. Differently, the variance coefficient σ (second plot) is only slightly affected by the flow Reynolds number, while it is strongly influenced by the modification of the streamwise pressure gradient. More precisely, the stronger the pressure gradient the higher the *pdf* variance, once expressed in terms of Re_θ variation through the transition region. This is directly linked to the enhanced growth of the BL momentum thickness across the entire length of transition. In other words, the shortening of the transition region observed at higher pressure gradients in the physical streamwise coordinate (see Fig. 9) does not balance the increased growth of θ at the larger channel diffusion. Similar considerations hold for the Tu level variation, i.e., the higher the Tu level the higher the σ and the larger the Re_θ variation across transition.

Finally, the bottom plot of Fig. 10 synthesizes the effects of Re, the pressure gradient and the Tu level on the parameter η defining the skewness of the *pdf* distributions. The pressure gradient variation has the largest effects (see also Nolan and Zaki (2013)), with η varying from about zero for the flat plate-like conditions (AP = 0), up to about 4 for the strongest diffusion. Similarly, the increment of the Tu level leads to slightly larger skewness. On the contrary, varying the flow Reynolds number has smaller effects. The pressure gradient and the Tu level therefore play an important role in defining the length of transition (σ) and the distribution of the nucleation events across the entire transition region (η). On the other hand, the momentum thickness Reynolds number at the mid-transition position (i.e., μ) is mostly influenced by the flow Reynolds number and Tu level, with minor effects due to the pressure gradient variation observed for the present cases.

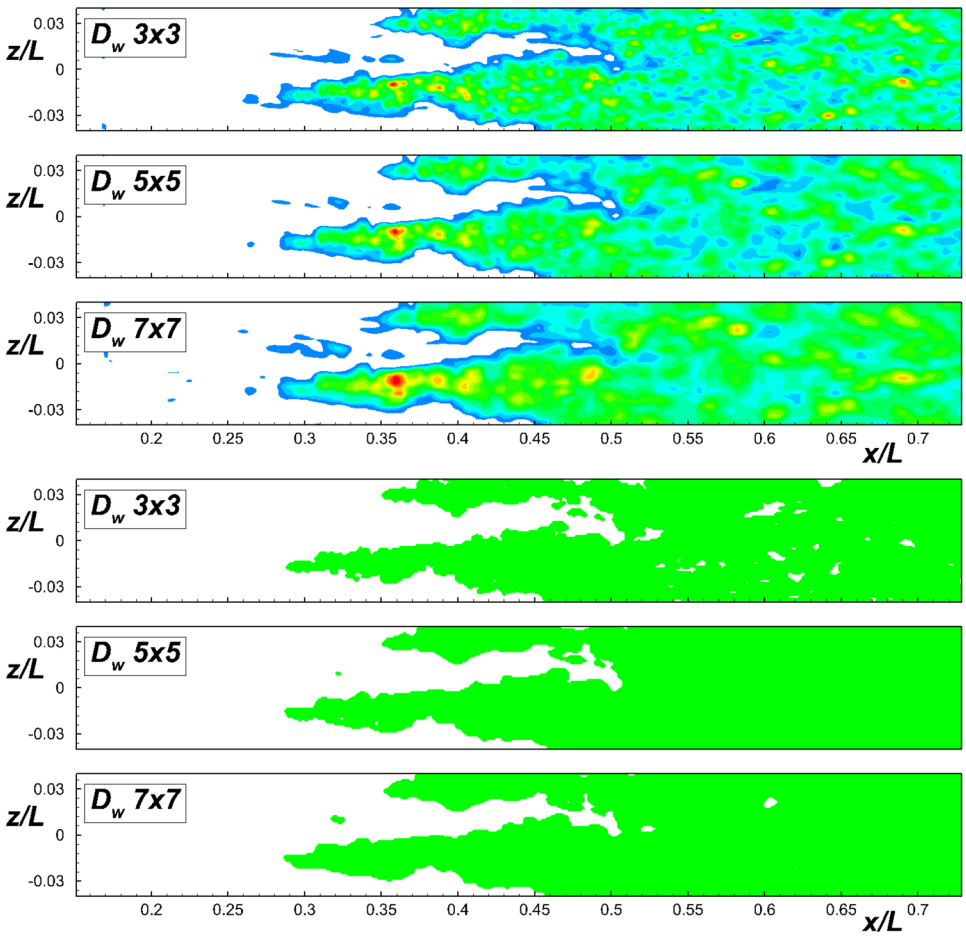

Fig. 11 Contour plots of D (top plots) and D_{binary} (bottom plots) for 3×3, 5×5 and 7×7 points cell, as computed from DNS data. Streamwise and spanwise coordinates are scaled with the plate length

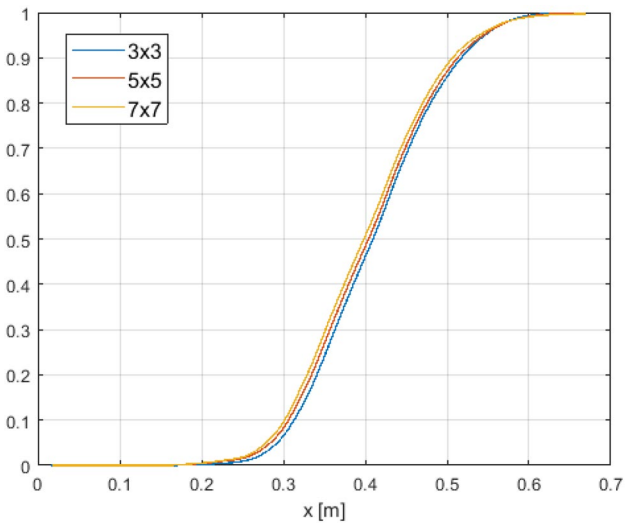

Fig. 12 Intermittency distributions for different cell sizes as computed from DNS data

6 Concluding remarks

The present work was aimed at providing a tool for the identification of turbulent spots in transitional boundary layers from PIV measurements, thus obtaining the statistical evolution of transition and the spot production rate. Detection functions for turbulent events recognition based on velocity data probed at about half of the boundary layer thickness are compared with a previously defined function based on the local wall-shear stress extracted from DNS data, which was already adopted in the literature.

The present results show that fluctuating velocity measured away from the wall within the boundary layer can be used as detectors for isolating turbulent regions in the boundary layer. Particularly, the signatures of turbulent spots and the laminar–turbulent interface in the boundary layer were correctly captured using the spanwise fluctuating velocity and its spatial derivatives as detection functions. Indeed, the intermittency curves and the spot production rate obtained from velocity data provided by DNS

at about half of the boundary layer thickness were found to be substantially superimposed to those obtained using the local wall-shear stress as detection function.

The application of the procedure presented in this work to PIV measurements highlighted the capability of the present method to capture the statistical response of the boundary layer to the modification of the Reynolds number, the *Tu* levels and the pressure gradient. As expected, the location of the maximum spot nucleation was shown to move upstream when increasing all the main flow parameters. Additionally, the transition region became shorter for higher *Re* and APG, whereas the *Tu* level variation had the opposite trend.

Finally, the inspection of the link between the coefficients defining the analytic distribution of the *pdf* of spot nucleation and the momentum thickness Reynolds number at the mid-transition position clearly showed the usability of the present method for providing correlations for transition prediction from experiments.

Appendix: sensitivity of D_{rms} and intermittency distributions on cell dimension

As it is pointed out in Sect. 4, the spatial rms of the detection function D was computed to further improve its sensitivity to turbulent fluctuations. The choice of the cell dimension relies on the spatial resolution compared to the length scales of velocity fluctuations in the observed flow field. A sensitivity analysis on the cell area has been done using DNS data, which is reported her in Figs. 11 and 12. The results for a 3×3, 5×5 and 7×7 points cell are reported in terms of the D_{rms} and the D_{bin} distributions (Fig. 11). As expected, increasing the cell size leads to a smoother distribution of these quantities. However, their general distributions and the capability of the present procedure to isolate turbulent spots forming in the boundary layer do not change significantly. This is further confirmed by the intermittency distributions depicted in Fig. 12 for the three analyzed cases. The curves are indeed substantially superimposed one another, and thus, the estimated transition start and end positions are the same. Otherwise, in the authors' opinion, a sensitivity analysis should be done in future works when adopting the present techniques based on the available numerical and experimental data.

Funding Open access funding provided by Università degli Studi di Genova within the CRUI-CARE Agreement.

Declarations

Conflicts of interest The authors declare that they have no conflict of interest

Consent for publication The authors report that they have consent for publication.

References

Abu-Ghannam B, Shaw R (1980) Natural transition of boundary layers-the effects of turbulence, pressure gradient, and flow history. J Mech Eng Sci 22(5):213–228

Azzazy M, Modarress D, Hall R (1989) Optical boundary-layer transition detection in a transonic wind tunnel. AIAA J 27(4):405–410

Batill SM, Mueller TJ (1981) Visualization of transition in the flow over an airfoil using the smoke-wire technique. AIAA J 19(3):340–345

Brandt L, Schlatter P, Henningson DS (2004) Transition in boundary layers subject to free-stream turbulence. J Fluid Mech 517:167–198

Chauhan K, Philip J, De Silva CM et al (2014) The turbulent/non-turbulent interface and entrainment in a boundary layer. J Fluid Mech 742:119–151

Dellacasagrande M, Lengani D, Simoni D et al (2020) Evaluation of turbulent spot production rate in boundary layers under variable pressure gradients for gas turbine applications. J Turbomach 142(6):061003

Dellacasagrande M, Lengani D, Simoni D et al (2021) Statistical characterization of free-stream turbulence induced transition under variable reynolds number, free-stream turbulence, and pressure gradient. Phys Fluids 33(9):094115

Dellacasagrande M, Verdoya J, Barsi D et al (2021) Mixed lse and epod based technique for multi-plane piv measurements synchronization in separated flow condition. Exp Thermal Fluid Sci 122(110):313

Dick E, Kubacki S (2017) Transition models for turbomachinery boundary layer flows: a review. Int J Turbomach Propuls Power 2(2):4

Collineau S, Brunet Y (1993) Detection of turbulent coherent motions in a forest canopy part i: Wavelet analysis. Bound-Layer Meteorol 65(4):357–379

Durović K (2022) Numerical studies of the transition in a flat-plate boundary layer under the influence of free-stream turbulence. PhD thesis, KTH Royal Institute of Technology

Durović K, De Vincentiis L, Simoni D et al (2021) Free-stream turbulence-induced boundary-layer transition in low-pressure turbines. J Turbomach 143(8):081015

Emmons HW (1951) The laminar-turbulent transition in a boundary layer-part I. J Aeronaut Sciences 18(7):490–498
Fischer PF, Lottes JW, Kerkemeier SG (2021) Nek5000.http://nek5000.mcs.anl.gov
Fransson JH, Matsubara M, Alfredsson PH (2005) Transition induced by free-stream turbulence. J Fluid Mech 527:1–25
Fransson JHM, Shahinfar S (2020) On the effect of free-stream turbulence on boundary-layer transition. J Fluid Mech 899:A23
Gardner A, Eder C, Wolf C et al (2017) Analysis of differential infrared thermography for boundary layer transition detection. Exp Fluids 58(9):1–14
Gostelow J, Blunden A, Walker G (1992) Effects of free-stream turbulence and adverse pressure gradients on boundary layer transition. In: ASME 1992 International Gas Turbine and Aeroengine Congress and Exposition, American Society of Mechanical Engineers, pp V001T01A128–V001T01A128
Green MA, Rowley CW, Haller G (2007) Detection of lagrangian coherent structures in three-dimensional turbulence. J Fluid Mech 572:111–120
Havener AG (1977) Detection of boundary-layer transition using holography. AIAA J 15(4):592–593
Heisel M, Dasari T, Liu Y et al (2018) The spatial structure of the logarithmic region in very-high-reynolds-number rough wall turbulent boundary layers. J Fluid Mech 857:704–747
Herbert T (1991) Boundary-layer transition-analysis and prediction revisited. In: 29th Aerospace Sciences Meeting, p 737
Kreilos T, Khapko T, Schlatter P et al (2016) Bypass transition and spot nucleation in boundary layers. Phys Rev Fluids 1(4):043602
Kwon Y, Hutchins N, Monty J (2016) On the use of the reynolds decomposition in the intermittent region of turbulent boundary layers. J Fluid Mech 794:5–16
Lee J, Zaki T (2017) Signature of large-scale motions on turbulent/non-turbulent interface in boundary layers. J Fluid Mech 819:165–187
Lee J, Zaki TA (2018) Detection algorithm for turbulent interfaces and large-scale structures in intermittent flows. Comput Fluids 175:142–158
Mans J, Kadijk EC, de Lange HC et al (2005) Breakdown in a boundary layer exposed to free-stream turbulencel. Exp Fluids 39:1071–1083
Matsubara M, Alfredsson PH (2001) Disturbance growth in boundary layers subjected to free-stream turbulence. J Fluid Mech 430:149–168
Mayle RE (1991) The role of laminar-turbulent transition in gas turbine engines. J Turbomach 113:509–537
Menter FR, Langtry RB, Likki S et al (2006) A correlation-based transition model using local variables-part I: model formulation. J Turbomach 128(3):413–422
Morkovin MV (1969) On the many faces of transition. In: Wells CS (ed) Viscous drag reduction. Springer, Boston, pp 1–31. https://doi.org/10.1007/978-1-4899-5579-1_1
Narasimha R, Devasia K, Gururani G et al (1984) Transitional intermittency in boundary layers subjected to pressure gradient. Exp Fluids 2(4):171–176
Nolan K, Zaki T (2013) Conditional sampling of transitional boundary layers in pressure gradients. J Fluid Mech 728:306–339
Ohno D et al (2022) Investigations of laminar to turbulent transition in an oscillating airfoil boundary layer. In: IUTAM Laminar-Turbulent Transition. Springer, Cham, pp 469–478
Ol'Shanskii M, Staroverov VM (2000) On simulation of outflow boundary conditions in finite difference calculations for incompressible fluid. Int J Numer Meth Fluids 33(4):499–534
Otsu N (1979) A threshold selection method from gray-level histograms. IEEE Trans Syst Man Cybern 9(1):62–66
Ovchinnikov V, Choudhari MM, Piomelli U (2008) Numerical simulations of boundary-layer bypass transition due to high-amplitude free-stream turbulence. J Fluid Mech 613:135–169
Parziale N, Shepherd J, Hornung H (2013) Differential interferometric measurement of instability in a hypervelocity boundary layer. AIAA J 51(3):750–754
Patera AT (1984) A spectral element method for fluid dynamics: laminar flow in a channel expansion. J Comput Phys 54(3):468–488
Reuther N, Kähler CJ (2018) Evaluation of large-scale turbulent/non-turbulent interface detection methods for wall-bounded flows. Exp Fluids 59(7):1–17
Richter K, Schülein E (2014) Boundary-layer transition measurements on hovering helicopter rotors by infrared thermography. Exp Fluids 55(7):1–13
Richter K, Wolf CC, Gardner A, et al (2016) Detection of unsteady boundary layer transition using three experimental methods. In: 54th AIAA aerospace sciences meeting, p 1072
Satta F, Simoni D, Ubaldi M et al (2007) Velocity and turbulence measurements in a separating boundary layer with and without passive flow control. Proc Inst Mech Eng Part A J Power Energy 221(6):815–818
Scarano F, Benocci C, Riethmuller M (1999) Pattern recognition analysis of the turbulent flow past a backward facing step. Phys Fluids 11(12):3808–3818
Schlatter P (2001) Direct numerical simulation of laminar-turbulent transition in boundary layer subject to free-stream turbulence. Master's thesis, ETH, Zürich, Switzerland
Schulte V, Hodson HP (1998) Unsteady wake-induced boundary layer transition in high lift LP turbines. J Turbomach 120(1):28–35
Sciacchitano A, Neal DR, Smith BL et al (2015) Collaborative framework for piv uncertainty quantification: comparative assessment of methods. Meas Sci Technol 26(7):074004
Siddiqui ME, Mukund V, Scott J et al (2013) Experimental characterization of transition region in rotating-disk boundary layer. Physics of Fluids 25(3):034102
Simoni D, Lengani D, Guida R (2016) A wavelet-based intermittency detection technique from PIV investigations in transitional boundary layers. Exp Fluids 57(9):145
Tillmark N, Alfredsson PH (1992) Experiments on transition in plane couette flow. J Fluid Mech 235:89–102
Verdoya J, Dellacasagrande M, Lengani D et al (2021) Inspection of structures interaction in laminar separation bubbles with extended proper orthogonal decomposition applied to multi-plane particle image velocimetry data. Phys Fluids 33(4):043607
Weiss A, Wolf CC, Kaufmann K et al (2020) Unsteady boundary-layer transition measurements and computations on a rotating blade under cyclic pitch conditions. Exp Fluids 61(2):1–16
Wieneke B (2015) PIV uncertainty quantification from correlation statistics. Meas Sci Technol 26(7):074002
Zaki T (2013) From streaks to spots and on to turbulence: Exploring the dynamics of boundary layer transition. Flow Turbul Combust 91:451–473